

Time-evolving coronal modelling of solar maximum around the May 2024 storm by COCONUT

H. P. Wang¹, S. Poedts^{1,2}, A. Lani^{1,3}, L. Linan¹, T. Baratashvili¹, F. Zhang^{4,5}, D. Sorokina¹, H.-J. Jeong^{1,6}, Y. C. Li¹, M. Najafi-Ziyazi¹, and B. Schmieder^{1,7,8}

¹ Centre for Mathematical Plasma-Astrophysics, Department of Mathematics, KU Leuven, Celestijnenlaan 200B, 3001 Leuven, Belgium

e-mail: Stefaan.Poedts@kuleuven.be

e-mail: andrea.lani@kuleuven.be

e-mail: haopeng.wang1@kuleuven.be

² Institute of Physics, University of Maria Curie-Skłodowska, ul. Radziszewskiego 10, 20-031 Lublin, Poland

³ Von Karman Institute For Fluid Dynamics, Waterloosesteenweg 72, 1640 Sint-Genesius-Rode, Brussels, Belgium

⁴ Institute of Theoretical Astrophysics, University of Oslo, PO Box 1029 Blindern, 0315 Oslo, Norway

⁵ Rosseland Centre for Solar Physics, University of Oslo, PO Box 1029 Blindern, 0315 Oslo, Norway

⁶ School of Space Research, Kyung Hee University, Yongin, 17104, Republic of Korea

⁷ Observatoire de Paris, LIRA, UMR8254 (CNRS), F-92195 Meudon Principal Cedex, France

⁸ SUPA, School of Physics & Astronomy, University of Glasgow, Glasgow G12 8QQ, UK

June 12, 2025

ABSTRACT

Context. Time-evolving magnetohydrodynamic (MHD) coronal models driven by a sequence of time-evolving photospheric magnetograms deliver more realistic results than traditional quasi-steady-state models constrained by a static magnetogram. The fully implicit, time-evolving COCONUT (Wang et al. 2025b) performs efficiently enough for real-time coronal simulations during solar minimum. However, significant challenges persist in modelling the more complex coronal evolutions of the solar maximum.

Aims. During solar maximum, the coronal magnetic field is more complex and stronger, and coronal structures evolve more rapidly than during solar minimum. Consequently, time-evolving MHD coronal modelling of the solar maximum often struggles with poor numerical stability and low computational efficiency. This paper aims to enhance the numerical stability of the time-evolving COCONUT coronal model to mitigate these issues, to evaluate differences between the time-evolving and quasi-steady-state coronal simulation results, and to assess the impact of spatial resolution on global MHD coronal modelling of solar maximum.

Methods. After enhancing the positivity-preserving (PP) property of the time-evolving COCONUT coronal model, we employ it to simulate the evolution of coronal structures from the solar surface to 0.1 AU in an inertial coordinate system over two Carrington rotations (CRs) around the May 2024 solar storm event. These simulations are performed on unstructured geodesic meshes containing 6.06, 1.52, and 0.38 million (M) cells to assess the impact of grid resolution. We also conduct a quasi-steady-state coronal simulation, treating the solar surface as a rigidly rotating spherical shell, to demonstrate the impact of magnetic flux emergence and cancellation in global coronal simulations. Comparison with observations further validates the reliability of the efficient time-evolving coronal modelling technique.

Results. This paper demonstrates that incorporating magnetic field evolution in inner-boundary conditions can significantly improve the fidelity of global MHD coronal simulations around solar maximum. The simulated magnetic field strength using a refined mesh with 6.06 M cells can be more than 40% stronger than that in the coarser mesh with 0.38 M cells. A time step of 5 minutes and the mesh containing 1.5 M cells can effectively capture the evolution of large-scale coronal structures and small-sized dipoles. Thus, the fully implicit time-evolving COCONUT shows promise for accurately conducting real-time global coronal simulations of solar maximum, making it suitable for practical applications such as daily space weather forecasting.

Key words. Sun: magnetohydrodynamics (MHD) –methods: numerical –Sun: corona

1. Introduction

Space weather refers to the dynamic physical conditions on the Sun, in the solar wind, and within the Earth’s magnetosphere and ionosphere that can impact the performance and reliability of both space- and ground-based technological systems, as well as pose risks to human life and health. There is an urgent need to develop advanced physics-based magnetohydrodynamic (MHD) Sun-to-Earth model chains to understand the mechanisms of space weather and ultimately provide reliable space weather forecasts hours to days in advance (e.g. Baker 1998; Feng et al. 2011, 2013; Feng 2020; Koskinen et al. 2017).

However, MHD simulations of the solar–terrestrial system involve various physical phenomena spanning diverse spatiotemporal scales, posing significant challenges in achieving the high numerical stability and computational efficiency necessary for practical applications. We need to develop more efficient and reliable MHD solar-terrestrial models to improve space weather forecasting (e.g. Feng 2020; Owens et al. 2017, and references therein).

Most Sun-to-Earth model chains couple multiple models, each dedicated to specific regions and physical problems, to construct a comprehensive solar-terrestrial space weather fore-

casting framework (e.g. Feng et al. 2013; Goodrich et al. 2004; Hayashi et al. 2021; Odstrcil et al. 2004; Pomoell & Poedts 2018; Poedts, S. et al. 2020; Tóth et al. 2012). Among these models, the coronal model is essential for initializing other components and accurately simulating solar disturbances such as coronal mass ejections (CMEs) (Brchnelova et al. 2022; Kuźma et al. 2023; Perri et al. 2023). Moreover, physics-based MHD coronal models are typically the most complex and computationally intensive component of the Sun-to-Earth model chain (Wang et al. 2025a,b). As a result, the overall efficiency and reliability of the model chain are significantly determined by the performance of the coronal model.

Generally speaking, MHD coronal models can be categorized into three types. Steady-state coronal models, constrained by time-invariant magnetograms, aim to reproduce a stable coronal structure. Time-dependent coronal models are time-accurate and capable of capturing dynamic phenomena such as CME evolution within a stable coronal background constrained by a static magnetogram. However, using static magnetogram contradicts the inherently dynamic nature of the corona, which involves processes such as differential rotation, magnetic flux emergence, and cancellation. This simplification often leads to discrepancies between simulation results and observations (Cash et al. 2015; Owens et al. 2017; Réville et al. 2020). Time-evolving coronal models are both time-accurate and driven by a series of time-evolving magnetograms, allowing for the simulation of a more realistic and continuously evolving corona, an essential capability for the next generation of solar wind and CME modelling (Lionello et al. 2023). A more detailed description of these coronal models is available in Wang et al. (2025b).

Recently, implicit temporal discretization strategies have increased the computational efficiency of steady-state coronal simulations by enabling a time step exceeding the limitations imposed by the Courant-Friedrichs-Lewy (CFL) stability condition, achieving speed-ups of about one to two orders of magnitude compared to explicit models (Brchnelova et al. 2023a; Feng et al. 2021; Kuźma et al. 2023; Liu et al. 2023; Perri et al. 2018, 2022, 2023; Wang et al. 2019, 2022a,b, 2025a). Additionally, the temporal accuracy of implicit coronal models has been enhanced through the use of the second-order backward differentiation formula (BDF2) with Newton iterations at each time step, as well as the pseudo-time marching method, which introduces a pseudo-time dimension at each physical time step. These approaches enable the time-dependent coronal models constrained by static magnetograms to simulate CME evolution in the coronal region with required computational efficiency and temporal accuracy (Guo et al. 2023; Linan et al. 2023; Wang et al. 2025a). However, most time-evolving coronal models still rely on explicit or semi-implicit temporal integration methods (Feng et al. 2023; Hayashi et al. 2021; Hoeksema et al. 2020; Linker et al. 2024; Lionello et al. 2023; Mason et al. 2023; Yang et al. 2012), where the time-step size is constrained by the explicitly treated terms, making these simulations prohibitively computationally expensive for practical applications (Yeates et al. 2018).

To address the efficiency barrier in time-evolving coronal simulations, Wang et al. (2025b) made the first fully-implicit time-evolving MHD coronal model based on COolfluid COroNal Unstructured (COCONUT), a novel implicit MHD solar corona model based on Computational Object-Oriented Libraries for Fluid Dynamics (COOLFluid) (Kampe et al. 2005; Lani et al. 2005, 2013)¹. It is capable of performing real-time global coronal simulations during solar minima with 1.5 million

cells using no more than 20 CPU cores. However, it still faces challenges in resolving low- β issues, where non-physical negative thermal pressures may arise when deriving thermal pressure from energy density in low- β regions, as well as struggles with the development of very high-speed streams above the active regions (Kuźma et al. 2023). More numerically stable algorithms are required to simulate coronal evolutions during solar maxima.

The numerical stability of quasi-steady-state and time-dependent MHD coronal models constrained by static magnetograms has been significantly improved by adopting decomposed MHD equations (e.g. Feng et al. 2010, 2021; Li et al. 2018; Wang et al. 2019, 2022a,b, 2025a) in which the magnetic field \mathbf{B} is split into a time-dependent field \mathbf{B}_1 and a time-independent potential field (e.g., Fuchs et al. 2010; Guo 2015; Powell et al. 1999; Tanaka 1995), or more generally an arbitrary background field \mathbf{B}_0 (Xia et al. 2018). Furthermore, Wang et al. (2025c) proposed an extended MHD decomposition strategy and successfully implemented it in the time-evolving SIP-IFVM coronal model. It introduces a temporally piecewise-constant variable to accommodate part of the non-potential field, thereby ensuring that $|\mathbf{B}_1|$ remains sufficiently small throughout the simulation and improving the numerical stability of the time-evolving coronal model. However, implementing the extended MHD decomposition strategy in a global coronal model from scratch remains a non-trivial task.

Meanwhile, some researchers are trying to explore alternative approaches to enhance the numerical stability of MHD coronal models. Sokolov et al. (2021) updated the Alfvén Wave Wolar atmosphere Model (AWSoM) (Jin et al. 2017) by solving 1D equations for the plasma motion and heat transport along fixed potential magnetic field lines together with the Alfvénic wave propagation below $1.1 R_s$. Hoeksema et al. (2020) and Hayashi et al. (2021) switched to drive the coronal evolution below $1.15 R_s$ by a magneto-frictional (MF) model. The Magnetohydrodynamic Algorithm outside a Sphere (MAS) (MAS; Lionello et al. 2023; Linker et al. 2024; Mason et al. 2023), a state-of-the-art time-evolving MHD coronal model employing a semi-implicit approach, utilizes a zero- β approximation that neglects pressure and gravitational forces to generate energized magnetic fields (Yeates et al. 2018). Additionally, a specialized solution-preserving technique is employed to numerically bridge the photospheric magnetograms and the low corona, wherein the plasma density is artificially increased to broaden the transition region (Lionello et al. 2008; Mikić et al. 2013, 2018; Mok et al. 2005).

The methods mentioned above have the potential to enhance the numerical stability of the time-evolving COCONUT coronal model. As a newly developed, advanced MHD coronal model that benefits from an unstructured mesh and a fully implicit scheme, COCONUT provides an excellent platform for developing novel PP approaches prior to incorporating more established techniques. In Brchnelova et al. (2023b), the PP property of the COCONUT model was enhanced by adjusting the inner-boundary density to maintain the local Alfvénic velocity within appropriate ranges. Wang et al. (2025b) further extended this method to all the computational domains. Meanwhile, an HLL Riemann solver with a self-adjustable dissipation term Wang et al. (2025b) is proposed to improve numerical stability. Additionally, similar to the mass flux limitation strategies in Hayashi (2005) and Yang et al. (2012), the plasma velocity at the inner boundary is constrained so that it does not significantly exceed the characteristic velocities associated with supergranulation or sunspots (Wang et al. 2025b). Although these strategies perform well for simulating coronal evolution during solar minimum,

¹ <https://github.com/andrealani/COOLFluid/wiki>

they sometimes fail under solar maximum conditions. In this paper, we introduce additional PP algorithms to further enhance the time-evolving COCONUT model's capability to handle solar maximum coronal simulations.

During solar maxima, solar activity evolves significantly more rapidly compared to solar minima. This period is characterized by the frequent emergence of active regions (ARs), visible as sunspots, resulting from the shearing of magnetic fields by differential rotation and the subsequent rise of new magnetic flux through the convection zone (Brun & Browning 2017; Finley et al. 2024). Additionally, predominantly unipolar magnetic fields near the solar poles undergo a reversal in polarity during solar maxima (Brun et al. 2015). In addition, ARs emerging on the far side of the Sun, which cannot be captured well by single synoptic maps, have significant global effects on the magnetic structure (Perri et al. 2024). Given that Wang et al. (2025b) has demonstrated that time-evolving MHD coronal simulations can be performed efficiently and accurately using an implicit method, thereby offering a more realistic alternative to quasi-steady-state coronal simulations and that we have enhanced the numerical stability of COCONUT to address solar maximum conditions in this work, it is an opportune moment to compare quasi-steady-state and time-evolving coronal simulations of solar maximum. Such a comparison will illustrate the necessity and applicability of time-evolving MHD coronal simulations for practical space weather forecasting during the recent solar maximum of Solar Cycle 25.

At the onset of solar maximum in cycle 25, the strongest geomagnetic storm since November 2003 was triggered by NOAA AR 13664, the source of numerous CMEs and flares. Visible from Earth between May 2 and 14, 2024, AR 13664 evolved into one of the largest and most flare-productive active regions in recent decades. While these events have attracted considerable interest within the scientific community (Hayakawa et al. 2025; Jarolim et al. 2024; Kwak et al. 2024; Liu et al. 2024; Nedal et al. 2025), quasi-realistic MHD coronal simulations capturing the three-dimensional (3 D) evolution of global coronal structures during this period remain scarce. To address this gap, we performed coronal simulations that span two CRs around May 2024 solar event to validate COCONUT's capability for simulating time-evolving coronal structures during solar maximum.

Based on the above considerations, the paper is organized as follows. In Section 2, we introduce the numerical formulation of the time-evolving coronal model and describe the positivity-preserving (PP) measures used to enhance its numerical stability. In Section 3, we present the simulation results calculated by the time-evolving COCONUT coronal model, including the evolution of the corona during two solar maximum CR periods around the May 2024 solar storm. We compare the simulation driven by an artificially rotating static magnetogram with that driven by a sequence of hourly-updated time-evolving magnetograms, and we examine the effects of different grid resolutions. Finally, in Section 4, we summarize the key features of solar-maximum coronal modelling using the fully implicit, time-evolving corona model and give some concluding remarks.

2. Numerical algorithm

This section mainly describes the governing equations, grid system and inner-boundary conditions, and also presents the PP approach used to enhance the model's numerical stability.

2.1. The governing equations and grid system

As in Wang et al. (2025b) and Wang et al. (2025c), we perform time-evolving coronal simulations driven by a series of evolving magnetograms by solving the thermodynamic MHD equations in an inertial coordinate system. The governing equation is the same as in Wang et al. (2025b) and described as follows:

$$\frac{\partial \mathbf{U}}{\partial t} + \nabla \cdot \mathbf{F}(\mathbf{U}) = \mathbf{S}(\mathbf{U}, \nabla \mathbf{U}). \quad (1)$$

Here t is the time, \mathbf{U} represents the conservative variable vector, $\nabla \mathbf{U}$ denotes the spatial derivative of \mathbf{U} , $\mathbf{F}(\mathbf{U})$ is the inviscid flux vector, and $\mathbf{S}(\mathbf{U}, \nabla \mathbf{U}) = \mathbf{S}_{\text{gra}} + \mathbf{S}_{\text{heat}}$ represents the source term vector corresponding to the gravitational force and the heating source terms. The radiative loss term Q_{rad} , the coronal heating term Q_H , and the thermal conduction term $-\nabla \cdot \mathbf{q}$ are included in the heating source term \mathbf{S}_{heat} .

Q_{rad} and Q_H are defined the same as in Wang et al. (2025b). Originally, \mathbf{q} is defined in a Spitzer or collisionless form according to the radial distance as below (Hollweg 1978; Mikić et al. 1999):

$$\mathbf{q} = \begin{cases} -\xi T^{5/2} (\hat{\mathbf{b}} \cdot \nabla T) \hat{\mathbf{b}}, & \text{if } 1 \leq r \leq 10 R_s \\ \alpha n_e k_B T \mathbf{v}, & \text{if } r > 10 R_s \end{cases}. \quad (2)$$

Here r and T are the heliocentric distance and temperature of the bulk plasma, $R_s = 6.95 \times 10^8$ m is the solar radius, $k_B = 1.3806503 \times 10^{-23}$ J K⁻¹ denotes the Boltzmann constant, $\hat{\mathbf{b}} = \frac{\mathbf{B}}{|\mathbf{B}|}$, $\xi = 9.0 \times 10^{-12}$ J m⁻¹ s⁻¹ K^{-7/2}, α is set to $\frac{3}{2}$ (Lionello et al. 2008) and n_e is the electron number density. Additionally, $\mathbf{v} = (u, v, w)$ and $\mathbf{B} = (B_x, B_y, B_z)$ denote the velocity and magnetic fields in the Cartesian coordinate system. Considering that in the low corona there also exists regions with very weak magnetic fields where the heat flux may not remain aligned with the magnetic field, we hybridize the Spitzer form $\mathbf{q}_{\text{Spitzer}}$ with the collisionless form $\mathbf{q}_{\text{Collisionless}}$ based on the Alfvénic Mach number over the domain $1 R_s \leq r \leq 10 R_s$, as described in Eq. (3):

$$\mathbf{q} = \min\left(1, \frac{V_a}{|\mathbf{v}|}\right) \mathbf{q}_{\text{Spitzer}} + \left(1 - \min\left(1, \frac{V_a}{|\mathbf{v}|}\right)\right) \mathbf{q}_{\text{Collisionless}}, \quad (3)$$

where $V_a = \frac{|\mathbf{B}|}{\rho^{0.5}}$ is the Alfvén speed. Since abnormal high-speed flows, which usually indicates appearance of an energy imbalance, predominantly occur in low- β regions Wang et al. (2025c), we enhance the thermal conduction in these areas as follows:

$$\mathbf{q}^* = \mathbf{q} \left(1 + \tanh\left(\frac{1}{\beta} \cdot \frac{1}{100}\right)\right). \quad (4)$$

Furthermore, we apply a linear smoothing transition (Lionello et al. 2008; Mikić et al. 1999) between Eq. (4) and $\mathbf{q}_{\text{Collisionless}}$ over the domain of $10 R_s \leq r \leq 12.5 R_s$.

As usual, the Godunov method is adopted to advance the cell-averaged solution in time by solving a Riemann problem at each cell interface (Einfeldt et al. 1991; Godunov 1959). The computational domain is defined as a spherical shell spanning from 1.01 to around 25 R_s and is discretized into unstructured 5_{th} -, 6_{th} - and 7_{th} -level subdivided geodesic meshes (Brchnelova et al. 2022), which includes 378880, 1515520 and 6062080 non-overlapped prism cells, respectively. Each cell consists of 2 triangular faces and 3 quadrilateral faces. There are 74 layers of gradually stretched cells in the radial direction, each containing 5120, 20480 and 81920 cells, respectively. Given that the finest mesh resolution is approximately 1°, corresponding to roughly

100 minutes for the Sun to rotate through that angle, we adopt a time step of 5 minutes in all simulations, which is sufficient to capture the evolution of the main coronal structures (Wang et al. 2025b).

2.2. Implementation of boundary conditions

In this paper, all time-dependent coronal simulations begin with a steady-state solution constrained by a fixed magnetogram. In both steady-state and time-dependent coronal simulations, the observed GONG-zqs photospheric magnetograms provide the inner-boundary magnetic field (Li et al. 2021; Perri et al. 2023). We employ a potential field (PF) solver of 25th-order spherical harmonics expansion to extrapolate the photospheric magnetograms, where magnetic field strengths can reach several hundred Gauss near active regions, to the bottom of the low corona (Kuźma et al. 2023; Perri et al. 2022, 2023). Originally, the spherical harmonics expansion \mathcal{U} is expressed as

$$\mathcal{U} \approx \sum_{l=0}^{l_{\max}} \sum_{m=-l}^l I_l^m Y_l^m(\mu, \phi), \quad (5)$$

where Y_l^m denotes the spherical harmonic function of degree l and order m , I_l^m represents the corresponding spectral coefficient, $\phi \in [0, 2\pi)$ is the longitude, and $\mu \equiv \cos \theta$ with $\theta \in [0, \pi]$ denoting the colatitude.

Given that magnetic field strengths still exceed 50 Gauss and can lead to extremely low plasma β , resulting in non-physical negative temperatures or pressures and ultimately causing simulation failures, we apply a filter (McClarren & Hauck 2010) to \mathcal{U} . The filtered spherical harmonics expansion, $\mathcal{U}_{\text{filtered}}$, used in the PF reconstruction, is defined as

$$\mathcal{U}_{\text{filtered}} \approx \sum_{l=0}^{l_{\max}} \sum_{m=-l}^l \frac{I_l^m Y_l^m(\mu, \phi)}{1 + \xi l^2 (l+1)^2}, \quad (6)$$

where the filter strength $\xi = 1 \times 10^{-4}$ is adopted. This approach effectively limits the maximum magnetic field near the solar surface to approximately 30 Gauss during the simulation.

Meanwhile, the temperature and plasma density at the solar surface, denoted by T_s and ρ_s , are set to 1.8×10^6 K and 3.34×10^{-13} Kg m $^{-3}$, respectively. Correspondingly, the thermal pressure at the inner boundary is calculated as $p_s = 0.01$ Pa. The velocity vector and tangential magnetic field at the inner boundary, as well as the outer-boundary conditions are treated the same as in Wang et al. (2025b).

In the time-evolving coronal simulations, we drive the model using a series of hourly-updated GONG-zqs magnetograms², which have corrections at the poles to have a better estimate of the global magnetic flux (Perri et al. 2023). The simulations are performed in a quasi-inertial coordinate system, with the Earth permanently positioned at $\phi = 60^\circ$. For the quasi-steady-state coronal simulation, we rotate a static magnetogram to generate a series of hourly-updated magnetograms, which are then used to drive a rigidly rotating coronal structure. In both the quasi-steady-state and time-evolving simulations, the inner-boundary magnetic field at each time step is determined by applying a cubic Hermite interpolation to the four nearest hourly-updated input magnetograms.

² <https://gong.nso.edu/data/magmap/QR/zqs/202405/>

2.3. Positivity-preserving measures

Considering the presence of low- β regions ($\beta < 10^{-3}$) and rapid magnetic field evolution at the inner boundary during time-evolving coronal simulations performed in the inertial coordinate system, which can lead to non-physical negative thermal pressure due to discretization errors when deriving thermal pressure from energy density, we further implement some measures to ensure the PP property of the thermal pressure and density in the MHD simulations.

We define the inner-boundary plasma density ρ_{BC} and thermal pressure p_{BC} as follows (Brchnelova et al. 2023b; Wang et al. 2025b,c):

$$\begin{aligned} \rho_{BC} &= \Upsilon_\rho \frac{\mathbf{B}_{BC}^2}{V_{A,BCmax}^2} + (1 - \Upsilon_\rho) \rho_s, \\ p_{BC} &= \Upsilon_p \frac{\mathbf{B}_{BC}^2}{2} \beta_{\min} + (1 - \Upsilon_p) p_s \end{aligned}, \quad (7)$$

where $\Upsilon_\rho = 0.5 + 0.5 \cdot \tanh\left(\frac{V_A - V_{A,BCmax}}{V_{fac}} \cdot \pi\right)$ with $V_A = \frac{|\mathbf{B}_{BC}|}{\rho_s^{0.5}}$, $V_{A,BCmax} = 3000$ Km S $^{-1}$, and $V_{fac} = 2$ Km S $^{-1}$. For convenience of description, the magnetic field have already divided by $\sqrt{\mu_0}$ with $\mu_0 = 4 \times 10^{-7}$ π H m $^{-1}$ denoting the magnetic permeability. $\Upsilon_p = 0.5 + 0.5 \cdot \tanh\left(\frac{\beta_{\min} - \frac{ps}{0.5 \cdot \mathbf{B}_{BC}^2}}{\beta_{fac}} \cdot \pi\right)$ with $\beta_{fac} = 2 \times 10^{-6}$ and $\beta_{\min} = 10^{-3}$.

During time-dependent simulations, we use the BDF2 to calculate the temporal integration, with Newton iterations performed within each time step to update the intermediate solution states (Wang et al. 2025b). If the updated plasma density or thermal pressure falls beyond a threshold, in this paper $10^{-8} \rho_s < \rho < 10 \rho_s$ for the plasma density and $10^{-8} p_s < p < 100 p_s$ for the thermal pressure are adopted, we revert to the most recent valid value. The adoption of these thresholds is inspired by the PP reconstruction method in Feng et al. (2021) and Wang et al. (2022a), which limited the reconstructed density and pressure within this permitted interval. Furthermore, we appropriately adjust the plasma density and thermal pressure updated at each Newton iteration as below:

$$\begin{aligned} p &= \Upsilon_p \frac{\mathbf{B}^2}{2} \beta_{\min} + (1 - \Upsilon_p) p_o \\ \rho &= \Upsilon_\rho \frac{\mathbf{B}^2}{V_{A,max}^2} + (1 - \Upsilon_\rho) \rho_o \end{aligned}, \quad (8)$$

where p_o and ρ_o are the originally updated thermal pressure and plasma density, and $V_{A,max} = 2 \frac{|\mathbf{B}|_{max}}{\rho_s^{0.5}}$ with $|\mathbf{B}|_{max} = \max_{\text{Vcells}} |\mathbf{B}|$. Additionally, inspired by Wang et al. (2025c), we constrain the plasma velocity in the range of $1 R_s \leq r \leq 1.1 R_s$ not to exceed the speed of sound $C_s = \frac{\gamma p_i}{\rho_i}$, as described below:

$$\mathbf{v} = \mathbf{v}_o \cdot \min\left(\frac{C_s}{|\mathbf{v}_o|} \cdot \left(0.3 + \tanh\left(\frac{r - R_s}{R_s} \cdot 8.68\right)\right), 1.0\right), \quad (9)$$

where \mathbf{v}_o is the originally updated velocity in the Newton iteration.

3. Numerical results

In this section, we employ the time-evolving coronal model with enhanced numerical stability to simulate the evolution of coronal structures during CRs 2283 and 2284 which cover the period of

the May 2024 solar event. As mentioned in Subsection 2.1, the simulations are performed in a quasi-inertial coordinate system with Earth fixed at $\phi = 60^\circ$, adopting a 5-minute time step on the 5_{th} -, 6_{th} -, and 7_{th} -level geodesic meshes, respectively. Approximately 1300 hourly-updated GONG-zqs magnetograms from 5:00 on April 9, 2024, to 16:00 on June 2, 2024, are employed to drive these simulations. Figure 1 presents the distribution of the inner boundary magnetic field at four different moments in a co-rotating coordinate system.

In this paper, all calculations are performed on the WICE or genius cluster, part of the Tier-1 and Tier-2 supercomputer infrastructure of Vlaams Supercomputer Centrum (VSC)³. Using 900 CPU cores on the Tier-2 infrastructure and a time step of 5 minutes, the time-evolving coronal simulations run approximately 48 times and 9 times faster than real-time coronal evolution on the 6_{th} - and 7_{th} -level meshes, respectively. For the 5_{th} -level mesh, the simulation can be approximately 60 times faster than real-time evolution using only 270 CPU cores on Tier-2. In the following subsections, we present the results of the MHD coronal simulations for CRs 2283 and 2284.

3.1. Time-evolving versus quasi-steady-state coronal simulation results

In this subsection, we compare the results of the time-evolving simulation, driven by a series of hourly-updated magnetograms, with those from the quasi-steady-state simulation. As described in Subsection 2.2, the latter is constrained by a rigidly rotating magnetogram at 11:00 on May 6, 2024, a moment marking the end of CR 2283 and the beginning of CR 2284 and during the May 2024 solar storm period, which corresponds to the 654-th hour of the time-evolving simulation. All these simulation results presented in this subsection are calculated on the 6_{th} -level mesh. It shows that the temporal evolution of the magnetic field can lead to pronounced differences in simulation results.

Coronal holes (CHs) typically associated with low plasma density and magnetic field lines that are open to interplanetary space and are among the most prominent features of the solar corona (Petrie et al. 2011; Feng et al. 2015, 2017; Wang et al. 2025c). Polar CHs are located at the solar poles and often extend to lower latitudes, occasionally crossing the solar equator. Isolated CHs are detached from polar CHs and scattered across low- and mid-latitudes and are commonly observed near solar maxima. Transient CHs are associated with solar eruptive events, such as CMEs, solar flares, and eruptive prominences. In Fig. 2, we trace magnetic field lines to the solar surface to distinguish open- and closed-field regions, illustrating the pronounced changes of CHs during a solar maximum CR period.

Compared with magnetic field distribution between the 258-th and 570-th hours in Fig. 1, it can be seen that the emergence of positive magnetic field regions, with polarity opposite to the background, around $(75^\circ \text{ N}, 175^\circ)$ and $(18^\circ \text{ S}, 348^\circ)$, as well as the disappearance of such a region around $(10^\circ \text{ N}, 7^\circ)$, are well captured in the simulation results at the 570-th hour. It is also noted that, although the region with magnetic polarity opposite to the background around $(75^\circ \text{ N}, 175^\circ)$ becomes very small by the 876-th hour, it is still captured by the time-evolving coronal model. Additionally, the small-sized dipole that appears around $(18^\circ \text{ N}, 350^\circ)$ at the 876-th hour, as well as the dipole around $(26^\circ \text{ N}, 37^\circ)$ at the 1158-th hour, is also well captured in the simulation results. These features correspond to a closed-field region within the isolated coronal hole around $(26^\circ \text{ S}, 335^\circ)$ at

the 876-th hour, and the disappearance of the upper-left portion of the extended CH around $(10^\circ \text{ N}, 40^\circ)$ at the 1158-th hour.

White-light polarized brightness (pB) images can reveal various large-scale coronal structures. High-density features, such as bipolar and pseudo-streamers, typically appear as bright regions in pB images, while low-density structures, such as coronal holes, are manifested as dark regions (Feng et al. 2015, 2017, 2019; Feng 2020). In Fig. 3, we compare white-light polarized brightness (pB) images synthesized from the time-evolving (middle) and quasi-steady-state (bottom) simulation results with observed pB images from the innermost coronagraph of the Sun Earth Connection Coronal and Heliospheric Investigation (SECCHI) instrument suite (top) onboard the Solar Terrestrial Relations Observatory Ahead (STEREO-A) spacecraft⁴ (Howard et al. 2008). The simulated pB images are viewed from the STEREO-A perspective and cover the region from 2.5 to $15 R_s$. The orange lines overlaid on these images represent the simulated magnetic field lines.

Fig. 3 shows that, at the 258-th hour, the time-evolving simulation successfully captures the bipolar streamers centred around 37° N , 2° N and 47° S at the west limb, as well as the bipolar streamer centred around 14° N at the east limb. However, the quasi-steady state simulation fails to reproduce the bipolar streamer centred around 2° N at the west limb. The observed bright structures near the south polar and centred around 30° S at the east limb are misrepresented in both simulations as a broad bright feature, approximately 40° wide, centred around 60° S at the east limb. At the 570-th hour, both simulations produce 4 bipolar streamers centred around 36° N , 7° S , and 34° S at the east limb and centred around 9° N at the west limb. Additionally, the four simulated bright structures, one at the west limb, two near both poles, and the bipolar streamer centred around 7° S at the east limb, capture the observed bright structures. At the 876-th hour, the time-evolving simulation captures two bipolar streamers centred around 35° N and 49° S at the west limb, as well as one centred around 4° N at the east limb. However, the quasi-steady simulation misses the bipolar streamer centred around 49° S at the west limb, and the one at the east limb is displaced significantly northward relative to observations. Additionally, the quasi-steady simulation produces a pseudo-streamer centred around 18° S at the west limb, which is not present in the time-evolving simulation. Nevertheless, both simulations generally reproduce two broad bright structures near the two solar poles, in agreement with the observed features. At the 1158-th hour, the bright structure centred around 56° S at the west limb in both simulations is slightly displaced southward in both simulations compared to observations, while the structure centred around 53° S at the east limb is reasonably well reproduced. However, the other three observed bright structures are not captured by either simulation, and the broad bright structure around the north pole in the simulations deviates significantly from the observed features.

This comparison indicates that the simulated plasma density is generally consistent with the observed bright structures, with the time-evolving simulation showing better agreement than the quasi-steady simulation. The discrepancies in the width and position of these bright structures between observations and simulation may come from the imperfect measurements of photospheric magnetic fields, lack of direct observation of polar magnetic field, and limitation of the synoptic magnetograms in which the magnetic field at different longitudes is observed at different times (Hamada et al. 2018).

³ <https://www.vscentrum.be/>

⁴ <https://stereo-ssc.nascom.nasa.gov/browse/>

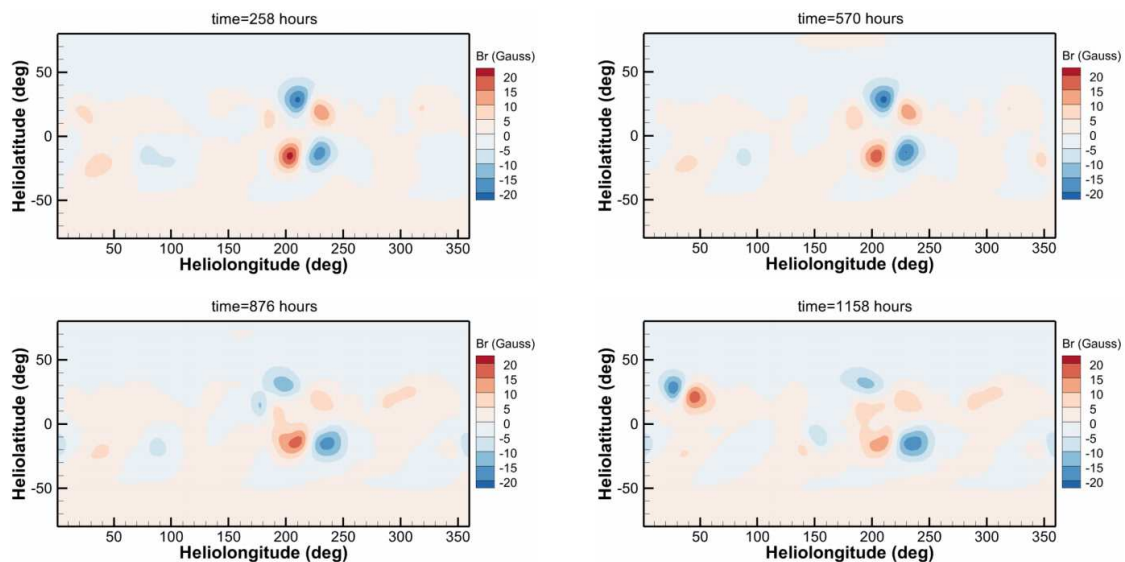


Fig. 1. Distribution of the radial magnetic field used as the inner boundary condition at the solar surface, shown in a co-rotating coordinate system.

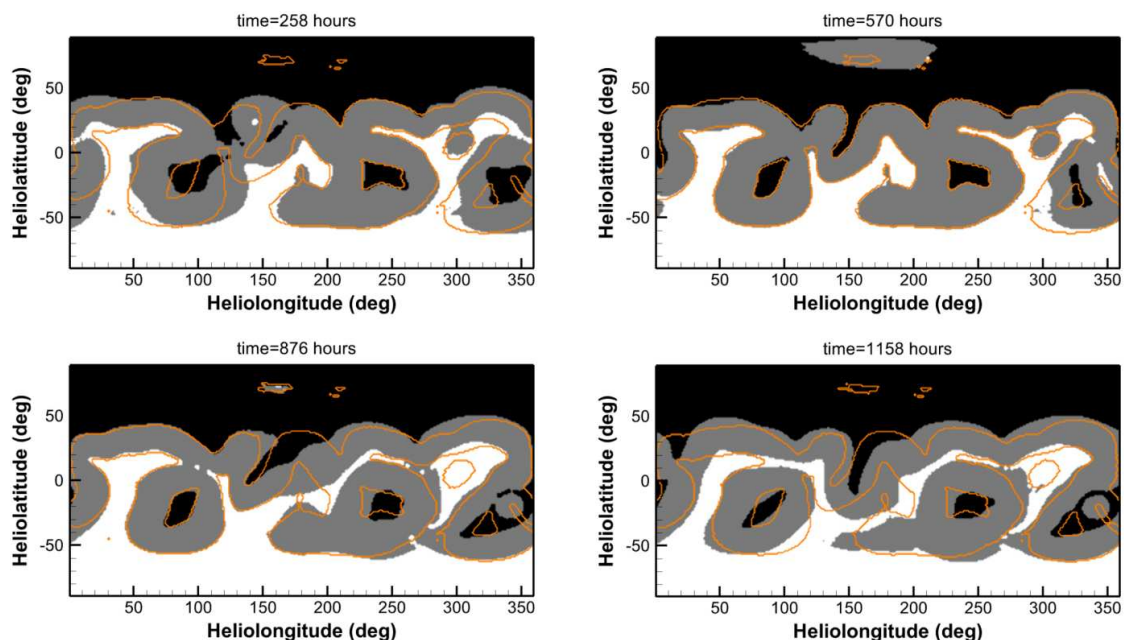


Fig. 2. Distributions of open- and closed-field regions derived from the time-evolving (contours) and quasi-steady-state (orange lines) simulation results. All shown in a co-rotating coordinate system, and the white and black patches represent open-field regions with magnetic field lines pointing outward and inward relative to the Sun, respectively, while the grey patches indicate closed-field regions. The orange solid lines overlaid on these contours denote the edge of close-field regions derived from the quasi-steady-state simulation results.

In Fig. 4, we further present synoptic maps of the east-limb (left) and west-limb (right) observations from the Large Angle and Spectrometric Coronagraph C2 (LASCO-C2) (Brueckner et al. 1995) onboard the Solar and Heliospheric Observatory (SOHO)⁵ for CRs 2284 and 2283, respectively. The west-limb and east-limb white-light pB images for CR 2283 and CR 2284 were synthesized from observations taken between April 16, 2024, and May 13, 2024, and between April 29, 2024, and May 26, 2024, respectively. These correspond to periods of 162-th to 816-th hours and 492-th to 1142-th hours in the time-evolving

simulations. The orange dashed and gray solid lines overlaid on these images represent the simulated magnetic neutral lines (MNLs), corresponding to the same positions and time periods as the observations, derived from the time-evolving and quasi-steady-state simulation results, respectively.

Fig. 4 shows that, in the west-limb pB image, the MNL in both the time-evolving and quasi-steady-state simulations coincide with the observed bright structures from 10° to 180° , and from 210° to 240° in longitude. However, the MNL from the time-evolving simulation is more consistent with these observed bright structures from 10° to 40° and from 315° to 360° . In the east-limb image, the MNL in the time-evolving simulation ex-

⁵ <https://sdo.gsfc.nasa.gov/data/synoptic/>

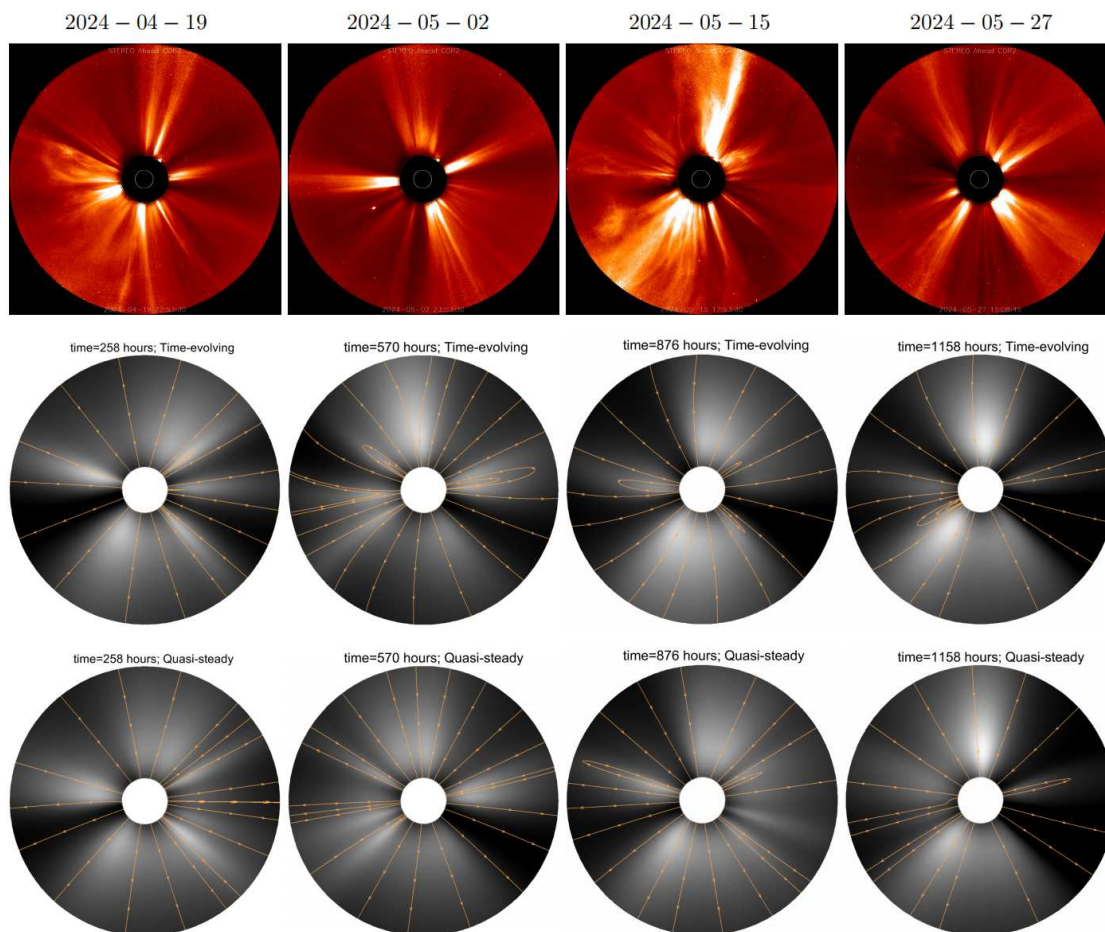


Fig. 3. White-light pB images observed from COR2/STEREO-A (top) and synthesized from quasi-steady-state (middle) and time-evolving (bottom) coronal simulation results ranging from 2.5 to $15 R_s$ on the meridian planes in the STEREO-A view. Orange lines highlight magnetic field lines on these selected meridional planes.

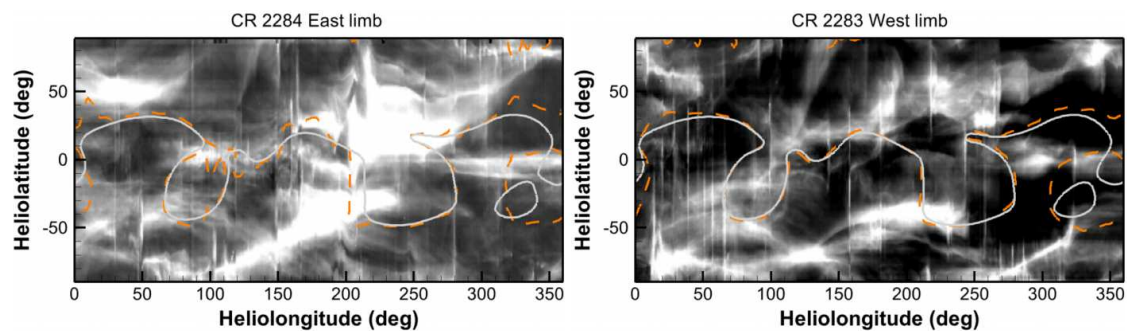


Fig. 4. Synoptic maps of east-limb (left) and west-limb (right) white-light pB observations from the SOHO instrument LASCO C2 at $3 R_s$ for CRs 2284 and 2283, respectively. The dashed orange line and solid gray line represent the corresponding magnetic neutral lines (MNLs) derived from the time-evolving and quasi-steady-state simulations, respectively.

tends farther north around 10° and 170° in longitude, crosses the region near 5° N from 90° to 115° , and vertically spans from 10° N to 50° S in latitude, providing a closer match to the observations than the quasi-steady-state simulation.

In Fig. 5, we present the 2 D timing diagrams of plasma density, velocity, and temperature at $21.5 R_s$, derived from the time-evolving simulation results during CRs 2283 and 2284. These images are plotted along the latitudes intersected by the Sun–Earth line. The orange dashed lines and the gray solid lines

denote the corresponding MNLs derived from the time-evolving and quasi-steady-state simulation results, respectively. It reveals that the MNL is generally coincidence with the latitude distribution of high-density low-speed solar wind. The distribution of the simulated plasma temperature is positively correlated with radial solar wind speeds (Elliott et al. 2012; Pinto & Rouillard 2017; Li et al. 2018), with the fast solar wind ($V_r > 550 \text{ km s}^{-1}$) exhibiting temperatures ranging from 1.1 to 1.8 MK, while the slow wind ($V_r < 450 \text{ km s}^{-1}$) corresponds to temperatures be-

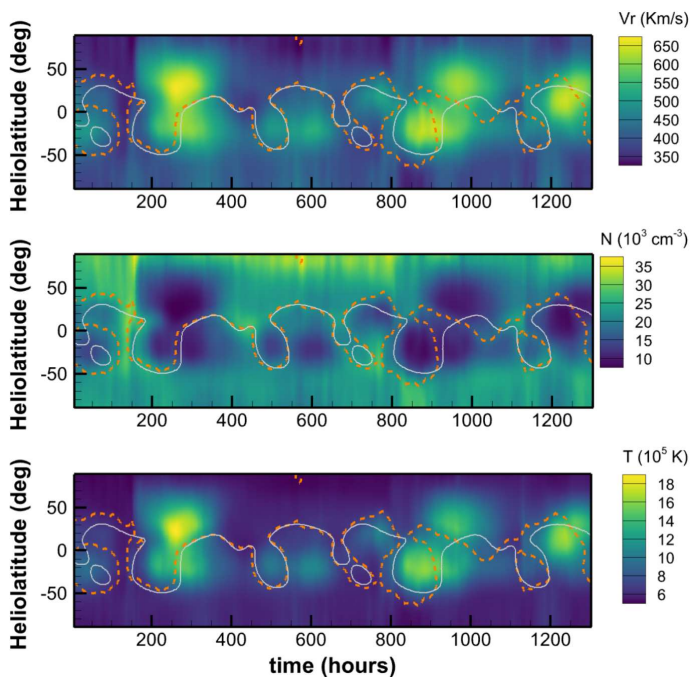


Fig. 5. Timing diagrams of simulated radial velocity V_r (km s^{-1} , top), plasma number density (10^3 cm^{-3} , middle), and temperature (10^5 K , bottom) along the latitudes intersected by the Sun–Earth line at 0.1 AU. The dashed orange line and solid gray line represent the corresponding magnetic neutral lines derived from the time-evolving and quasi-steady-state simulations, respectively.

tween 0.4 and 0.8 MK. However, during the intervals between the 260-th and 320-th hours, around the 930-th hour, and between the 1240-th and 1280-th hours, the MNL is accompanied with low-density, high-speed flows. This may be attributed to the absence of a self-consistent heating mechanism in this model.

Additionally, it is noticed that the evolution of MNLs in the time-evolving and quasi-steady-state simulations closely coincides between the 300-th and 650-th hours, but drifts apart thereafter. This agreement is attributed to the fact that the magnetic fields at latitudes west of the one intersected by the Sun–Earth line (Hamada et al. 2018) at the 654-th hour, the reference time for the synoptic magnetogram used in the quasi-steady-state simulation, are gradually updated during this time interval around the 300-th and 650-th hours. In contrast, the subsequent deviation is due to the absence of magnetic field evolution beyond this interval in the synoptic magnetogram used in the quasi-steady-state simulation.

3.2. The impact of grid resolutions on simulation results

In this subsection, we further evaluate the impact of grid cell sizes on the time-evolving coronal simulation results. We find that reducing the cell size in the tangential direction to one-quarter of that in the 5_{th} -level grid mesh, yielding a resolution a little higher than that of the synchronized magnetograms, leads to an increase of more than 40% in the simulated magnetic flux at 0.1 AU. The 6_{th} -level grid mesh achieves the desired accuracy in capturing large-scale coronal structures while maintaining high computational efficiency and numerical stability for global coronal simulations near solar maximum.

To enable comparison across unstructured meshes with different resolutions, the simulation results are first interpolated

onto a structured mesh with a resolution of 150×300 cells in the tangential direction. The interpolation is performed using the radial basis function (RBF) method proposed in Wang et al. (2022a), which is numerically stable, spatially accurate, and computationally efficient. All comparisons are conducted using the interpolated solutions on the structured mesh.

In Fig. 6, we display the distribution of open- and closed-field regions derived from the 876-th hours of the time-evolving simulation results on the 5_{th} - and 7_{th} -level subdivided geodesic meshes, respectively. Overlaid on these contours are the corresponding edge of the simulated open- and closed-field regions on the 6_{th} -level mesh. The polar CH regions on both the 5_{th} - and 7_{th} -level meshes coincide with those identified on the 6_{th} -level mesh. Besides, the 7_{th} -level mesh captures open-field regions at the lower left end of three isolated CHs centered around $(21^\circ\text{S}, 87^\circ)$, $(19^\circ\text{S}, 245^\circ)$ and $(29^\circ\text{S}, 335^\circ)$ and at the northern edge of the extended CH near $(10^\circ\text{N}, 100^\circ)$ and around $(50^\circ\text{S}, 265^\circ)$ that are missing on the 6_{th} -level mesh. In contrast, the open-field regions around these positions, as well as at the lower-left end of the isolated CH centered at $(7^\circ\text{N}, 305^\circ)$, appearing on the 6_{th} -level mesh, are absent from the 5_{th} -level mesh. It is also noticed the minor bipolar structure around $(70^\circ\text{N}, 160^\circ)$, displayed in Fig. 1, is well captured on 6_{th} - and 7_{th} -level meshes, but almost missed on the 5_{th} -level mesh.

In Fig. 7, we present the temporal evolution of radial velocity V_r (km s^{-1} ; a, d), proton number density N (10^5 cm^{-3} and 10^3 cm^{-3} ; b, e) and magnetic field strength $|\mathbf{B}|$ (G; c, f) at 3 (a, b, c) and $21.5 R_s$ (d, e, f). These parameters are monitored at the same solar latitude as Earth, but at a longitude that is lagging 60° , assuming that the solar wind takes approximately 100 hours to travel from 0.1 to 1 AU (Wang et al. 2025c). The black solid lines, black dashed lines, diamonds, and gray solid line denote the parameters derived from the time-evolving simulations on the 5_{th} -, 6_{th} - and 7_{th} -level subdivided geodesic meshes and observed by the WIND satellite at 1 AU, respectively. It reveals that a peak/trough in the plasma density profile generally corresponds to a trough/peak in the velocity profile in the three meshes. Moreover, the appearance times of the peak/trough in plasma density, radial velocity, and magnetic field strength coincided with each other in different meshes. However, both magnetic field strength and radial velocity are typically higher in the finer meshes, whereas plasma density tends to be lower. It is also noticed the radial velocity and plasma density values in the 7_{th} -level mesh closely match those in the 6_{th} -level mesh, except in the vicinity of peaks and troughs.

Additionally, the evolution pattern of radial velocity at 0.1 AU in the time-evolving simulations between the 400-th and 1050-th hours generally captures the observed radial velocity at 1 AU. However, the simulated velocity between the 400-th and 550-th hours is faster than the observations, while the simulated velocity peak between the 760-th and 820-th hours is noticeably slower. The simulated bi-peak in velocity around the 170-th hour may correspond to the observed bi-peak near the 290-th hour. However, the simulation at 0.1 AU fails to reproduce the observed low-speed flow at 1 AU between the 1100-th and 1300-th hours. These discrepancies may be attributed to several factors: the limitations of the empirical heating function used to approximate coronal heating and solar wind acceleration; inaccuracies in the synoptic magnetograms, where magnetic fields at different longitudes are observed at different times and polar magnetic fields are poorly measured, resulting in an incomplete representation of the actual magnetic field distribution; and the absence of transient phenomena such as coronal mass ejections, which are not included in the model but can significantly affect

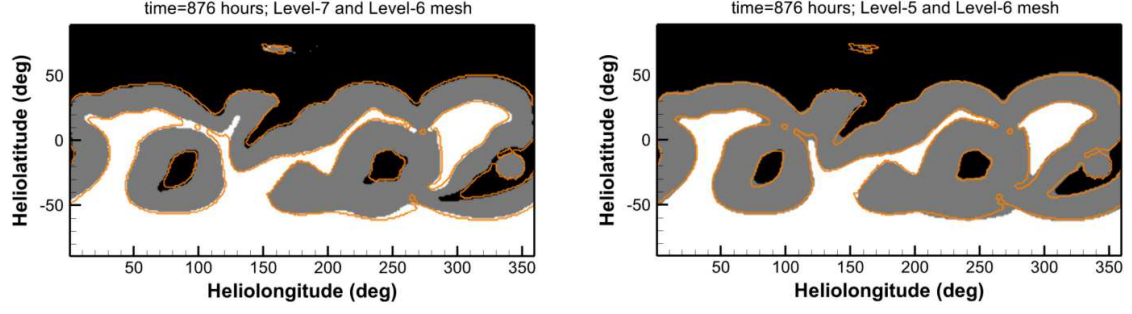


Fig. 6. Contours of open- and closed-field regions at the 876-th hour of the time-evolving simulations, performed on the 5_{th} - (left) and 7_{th} -level (right) subdivided geodesic meshes, respectively. The orange lines overlaid on these contours denote the edge of close-field regions derived from corresponding result on the 6_{th} -level mesh.

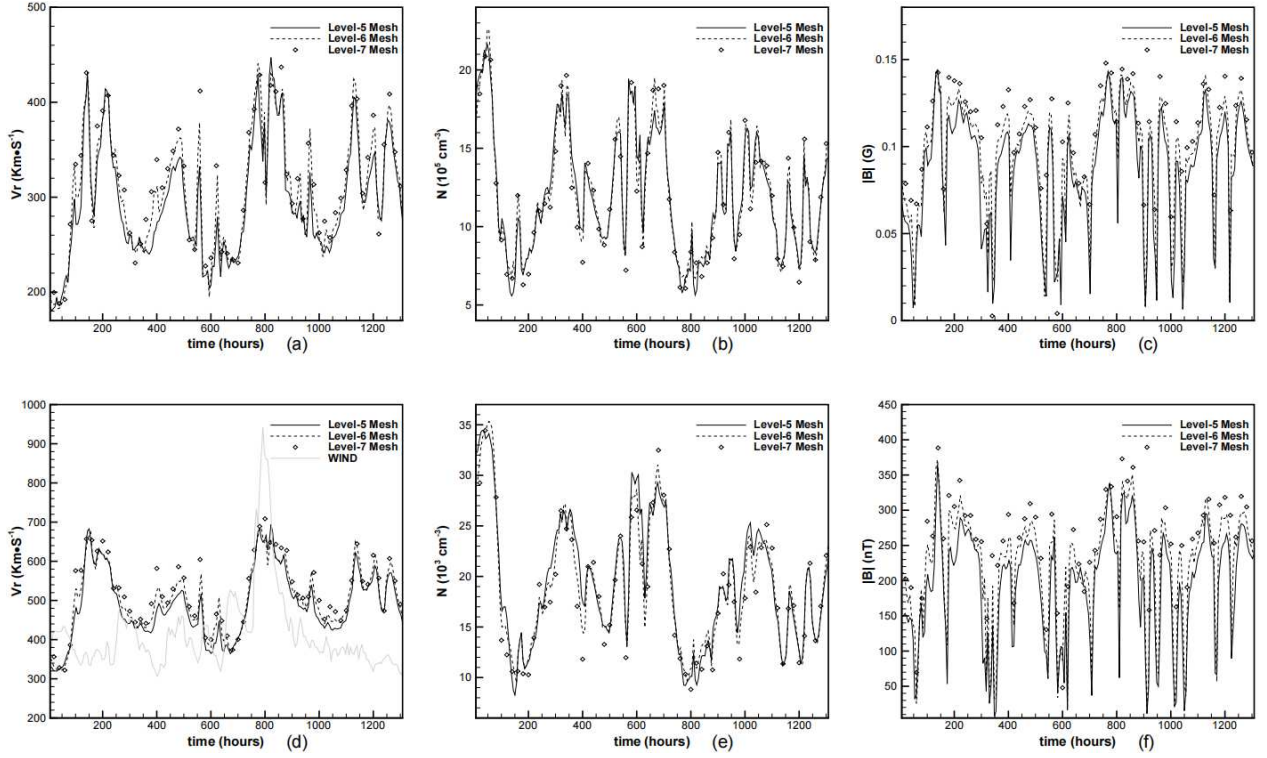


Fig. 7. Timing diagram of radial velocity V_r (km s^{-1} ; a, d), proton number density (10^5 cm^{-3} at $3 R_s$ and 10^3 cm^{-3} at $21.5 R_s$; b, e), and magnetic field strength $|\mathbf{B}|$ (G; c, f) observed by two virtual satellites located at $3 R_s$ (a, b, c) and $21.5 R_s$ (d, e, f), respectively. These virtual satellites are positioned at the same latitude as Earth but are lagged by 60° in longitude. The black solid lines, black dashed lines and diamonds represent the time-evolving simulation results on the 5_{th} -, 6_{th} - and 7_{th} -level subdivided geodesic meshes, respectively, while the gray solid line indicates the radial velocity observed by WIND satellite.

solar wind dynamics. Furthermore, during solar maximum, pronounced magnetic flux emergence and cancellation can produce complex solar wind structures that interact as they propagate from 0.1 AU to 1 AU, leading to substantial alterations in the solar wind structures.

In Table 1, we further list the average relative difference in solution variables between the results calculated on the K_{th} - and 5_{th} -level meshes, denoted as $\text{RD}_{\text{ave},\chi}^{\text{LV}_K}$,

$$\text{RD}_{\text{ave},\chi}^{\text{LV}_K} = \frac{1}{N^{\text{LV}_K}} \sum_{i=1}^{N^{\text{LV}_K}} \frac{\chi^{\text{LV}_K} - \chi^{\text{LV}_5}}{\chi^{\text{LV}_5}}.$$

Here, $\chi \in \{|\mathbf{B}|, \rho, V_r\}$ means the corresponding variable, N^{LV_K} denotes the number of sample points from the simulation

results on the N^{LV_K} -th level mesh, as shown in Fig. 7. For the 5_{th} - and 6_{th} -level meshes at $3 R_s$ and $21.5 R_s$, respectively, we selected 218 sample points with a 6-hour interval between two adjacent points. Because the 7_{th} -level mesh output files are extremely large (~ 1.7 GB each), we only selected 65 sample points with a 20-hour cadence. The subscript “ LV_K ” refers to the corresponding variables in the K_{th} -level mesh. It can be seen that the simulated magnetic field strength from the 6_{th} - and 7_{th} -level meshes is more than 20% and 40% stronger, respectively, than that calculated on the 5_{th} -level mesh at 0.1 AU. It is also noticed that this enhancement in magnetic field strength on finer meshes is more pronounced at $21.5 R_s$ than at $3 R_s$. Accordingly, the radial velocity increases and the plasma density decreases in the

Table 1. Average relative differences between variables calculated on the N_{th} - and 5_{th} -level meshes.

Parameters	$LV_N=6$	$LV_N=7$
$RD_{ave, B }^{LV_N}$ at $3 R_s$	21.96%	35.08%
$RD_{ave, B }^{LV_N}$ at $21.5 R_s$	23.78%	43.32%
$RD_{ave,\rho}^{LV_N}$ at $3 R_s$	0.50%	-1.17%
$RD_{ave,\rho}^{LV_N}$ at $21.5 R_s$	-1.90%	-4.37%
$RD_{ave,V_r}^{LV_N}$ at $3 R_s$	3.70%	6.94%
$RD_{ave,V_r}^{LV_N}$ at $21.5 R_s$	3.22%	6.83%

finer mesh, although these fluctuations are less pronounced than the enhancement in magnetic field strength.

These results indicate that the refined mesh can capture open-field regions missed by the coarser mesh, leading to a noticeable increase in the simulated magnetic flux away from the solar surface. This, in turn, affects the simulated flow field, typically resulting in an increase in radial velocity and a decrease in plasma density, although the magnitude of the average relative difference is approximately an order of magnitude lower than that observed in the magnetic field strength.

4. Concluding remarks

Recently, Wang et al. (2025b) established the first fully-implicit time-evolving MHD coronal model, capable of performing more than 70 times faster than real-time global coronal evolutions during a solar minimum (using 1080 CPU cores for 1.5M grid cells). However, the model still suffers from poor numerical stability and usually crashes in coronal simulations around solar maximum, where the magnetic field is stronger and more complex, and coronal structures evolve more rapidly. In this paper, we further improve its PP property to enable efficient computation of time-evolving coronal evolution during solar maximum and drive this model by about 1300 hourly-updated GONG-zqs magnetograms to simulate coronal evolutions during two CRs around the May 2024 solar storm event.

A comparison between the time-evolving coronal simulation and a quasi-steady-state simulation driven by a rigidly rotating magnetogram demonstrates that the temporal evolution of the magnetic field during a solar maximum CR can lead to significant differences in simulation results. Magnetic flux emergence and cancellation result in noticeable shifts, disappearances, and appearances of high-density streamers in white-light pB images. The MNL in the time-evolving simulation aligns more closely with the observed bright structures in the synoptic maps of pB images, and the evolution of magnetic field distributions on the solar surface are well captured by the simulated time-evolving 3D magnetic field structures. Additionally, the time-evolving simulation produces pronounced differences in the MNL at 0.1 AU compared to the quasi-steady-state simulation, demonstrating that the evolution of the inner-boundary magnetic field within a CR can lead to significant changes in the latitudinal structures of the solar wind at 0.1 AU.

Furthermore, a comparison between the time-evolving simulation results on the 5_{th} -, 6_{th} -, and 7_{th} -level meshes demonstrates that mesh refinement enables the model to capture the missed open-field regions in coarser meshes. When the resolution is increased by a factor of four, from the 5_{th} - to the 7_{th} -level mesh, the

simulated magnetic flux away from the solar surface increases by more than 40%. Although the changes in radial velocity and plasma density are less pronounced than those in magnetic flux, they exhibit corresponding increases and decreases, respectively. Also, this comparison, together with the figures demonstrating the evolution of open- and closed-field regions on the 6_{th} -level mesh, shows that the 6_{th} -level mesh can well capture the evolution of small-sized dipoles, as well as the emergence of small-sized magnetic field regions with polarity opposite to the background.

Additionally, given that both the finest mesh resolution and the distance between adjacent magnetic field pixels in the observed magnetograms are approximately 1° , corresponding to about 100 minutes of solar rotation, a time step of 5 minutes is sufficient to capture the evolution of the coronal structures with adequate temporal resolution in global coronal simulations. Considering that this model can perform about 48 and 9 times faster than real-time coronal evolution using 900 CPU cores on the 6_{th} - and 7_{th} -level meshes, respectively, we can conclude that a time step of 5 minutes and the 6_{th} -level mesh can generally balance computational efficiency, temporal accuracy, and numerical stability for global coronal simulations near solar maximum. This fully-implicit time-evolving MHD coronal model with improved PP property is promising for timely and accurately simulating the time-evolving coronal structures in daily practical space weather forecasting around solar maximum.

However, several challenges remain to be addressed for further improvement of this novel time-evolving implicit MHD coronal model. Given that the model can accurately capture the evolution of even small-scale dipolar structures observed in magnetograms through simulated 3D magnetic field evolution, it is essential to use synchronized magnetograms, where the magnetic fields across all longitudes are captured simultaneously (Upton & Hathaway 2014; Linker et al. 2024). This is necessary to overcome the limitations of current synoptic magnetograms, in which magnetic fields at different longitudes are observed at different times, resulting in significant deviations from the true magnetic field distributions. Extremely finer mesh comparable to the 9_{th} -level mesh, containing 16 times as much as grid cells on the 7_{th} -level mesh each layer, is still required to resolve the much faster, small-scale dynamics of active regions, such as sunspot rotation, to self-consistently simulate transient phenomena, including CME events triggered by sunspot rotation (Jiang et al. 2023), and to reduce diffusion due to numerical errors for capturing sufficiently thin current sheet (Jiang & Zhang 2025), in global MHD coronal simulations. Correspondingly, more stable and efficient numerical algorithms are still needed to deal with extremely low- β issues after considering these active-region evolutions. Additionally, physically consistent heating source terms are required to better simulate coronal heating and solar wind acceleration during time-evolving coronal simulations around solar maximum. Moreover, accurate measurements of the photospheric magnetic fields in the polar regions are necessary for reproducing more realistic coronal structures during solar maximum.

In our future work, we plan to simplify the novel extended MHD decomposition strategy proposed by Wang et al. (2025c) and implement it in the time-evolving COCONUT coronal model established in this paper. This improvement aims to further reduce the contamination of magnetic field discretization errors on thermal pressure derived from the total energy, consequently preventing the occurrence of non-physical negative thermal pressure values, which can lead the code to crash when dealing with low- β issues. Furthermore, we plan to implement local

mesh refinement, increasing the resolution to that of the 9th-level mesh only in regions containing active-region evolutions. This approach will enable self-consistent, faster-than-real-time simulations of CMEs triggered by sunspot rotation using the implicit time-evolving global MHD coronal model. Additionally, we plan to generate a series of synchronized magnetograms by incorporating surface flux transport models, such as the Advective Flux Transport (AFT) model (Upton & Hathaway 2014), with data from Solar Orbiter Polarimetric and Helioseismic Imager (Loeschl et al. 2024), horizontal velocities inferred from observational data using the time-distance helioseismology (Zhao et al. 2012; Yalim et al. 2017), and artificial intelligence-generated data from STEREO EUV observations (Jeong et al. 2020, 2022). This method has potential to generate a more realistic real-time magnetic field evolution at the inner boundary of our coronal model, leading to more accurate simulation results well match the observations around solar maximum. We also plan to couple this time-evolving coronal model with EUHFORIA, an inner heliospheric model, to further develop a quasi-realistic, faster-than-real-time Sun-to-Earth modelling chain suitable for practical daily space weather forecasting.

Acknowledgements. This project has received funding from the European Research Council Executive Agency (ERCEA) under the ERC-AdG agreement No. 101141362 (Open SESAME). These results were also obtained in the framework of the projects FA9550-18-1-0093 (AFOSR), C16/24/010 (C1 project Internal Funds KU Leuven), G0B5823N and G002523N (WEAVE) (FWO-Vlaanderen), and 4000145223 (SIDC Data Exploitation (SIDEEX), ESA Prodex). This work is also supported by the National Natural Science Foundation of China (grant No. 42030204) and the BK21 FOUR program of Graduate School, Kyung Hee University (GS-1-JO-NON-20242364). The resources and services used in this work were provided by the VSC (Flemish Supercomputer Centre), funded by the Research Foundation – Flanders (FWO) and the Flemish Government. The Research Council of Norway supports F.Z. through its Centres of Excellence scheme, project No. 262622. This work utilises data obtained by the Global Oscillation Network Group (GONG) program, managed by the National Solar Observatory and operated by AURA, Inc., under a cooperative agreement with the National Science Foundation. The data were acquired by instruments operated by the Big Bear Solar Observatory, High Altitude Observatory, Learmonth Solar Observatory, Udaipur Solar Observatory, Instituto de Astrofísica de Canarias, and Cerro Tololo Inter-American Observatory. The authors also acknowledge the use of the STEREO/SECCHI data produced by a consortium of the NRL (US), LMSAL (US), NASA/GSFC (US), RAL (UK), UBHAM (UK), MPS (Germany), CSL (Belgium), IOTA (France), and IAS (France).

References

- Baker, D. N. 1998, *Adv. Space Res.*, 22, 7
- Brchnelova, M., Kuźma, B., Perri, B., Lani, A., & Poedts, S. 2022, *ApJS*, 263, 18
- Brchnelova, M., Kuźma, B., Zhang, F., Lani, A., & Poedts, S. 2023a, *A & A*, 676
- Brchnelova, M., Kuźma, B., Zhang, F., et al. 2023b, *Sun Geosph.*, 15, 59
- Brchnelova, M., Zhang, F., Leitner, P., et al. 2022, *J. Plasma Phys.*, 88, 905880205
- Brueckner, G. E., Howard, R. A., Koomen, M. J., et al. 1995, *Sol. Phys.*, 162, 357
- Brun, A. S. & Browning, M. K. 2017, *Living Rev. Sol. Phys.*, 14, 4
- Brun, A. S., Browning, M. K., Dikpati, M., Hotta, H., & Strugarek, A. 2015, *Space Sci. Rev.*, 196, 101
- Cash, M. D., Biesecker, D. A., Pizzo, V., et al. 2015, *Space Weather*, 13, 611
- Einfeldt, B., Munz, C. D., Roe, P. L., & Sjogreen, B. 1991, *J. Comput. Phys.*, 92, 273
- Elliott, H. A., Henney, C. J., McComas, D. J., Smith, C. W., & Vasquez, B. J. 2012, *J. Geophys. Res.: Space Phys.*, 117
- Feng, X. S. 2020, *Magnetohydrodynamic Modeling of the Solar Corona and Heliosphere* (Singapore: Springer)
- Feng, X. S., Li, C. X., Xiang, C. Q., et al. 2017, *ApJS*, 233, 10
- Feng, X. S., Liu, X. J., Xiang, C. Q., Li, H. C., & Wei, F. S. 2019, *ApJ*, 871, 226
- Feng, X. S., Lv, J. K., Xiang, C. Q., & Jiang, C. W. 2023, *Mon. Not. R. Astron. Soc.*, 519, 6297
- Feng, X. S., Ma, X. P., & Xiang, C. Q. 2015, *J. Geophys. Res.: Space Phys.*, 120, 10,159
- Feng, X. S., Wang, H. P., Xiang, C. Q., et al. 2021, *ApJS*, 257, 34
- Feng, X. S., Xiang, C. Q., & Zhong, D. K. 2011, *Sci Sin-Terrae*, 41, 1
- Feng, X. S., Xiang, C. Q., & Zhong, D. K. 2013, *Sci Sin-Terrae*, 43, 912
- Feng, X. S., Yang, L. P., Xiang, C. Q., et al. 2010, *ApJ*, 723, 300
- Finley, A. J., Bru, A. S., Strugarek, A., & Cameron, R. 2024, *A & A*, 684, A92
- Fuchs, F. G., McMurry, A. D., Mishra, S., Risebro, N. H., & Waagan, K. 2010, *J. Comput. Phys.*, 229, 4033
- Godunov, S. K. 1959, *Mat. Sb. (N.S.)*, 1959, 271
- Goodrich, C., Sussman, A., Lyon, J., Shay, M., & Cassak, P. 2004, *J. Atmos. Sol.-Terr. Phys.*, 66, 1469, towards an Integrated Model of the Space Weather System
- Guo, J. H., Linan, L., Poedts, S., et al. 2023, *A & A*
- Guo, X. C. 2015, *J. Comput. Phys.*, 290, 352
- Hamada, A., Asikainen, T., Virtanen, I., & Mursula, K. 2018, *Sol. Phys.*, 293, 71
- Hayakawa, H., Ebihara, Y., Mishev, A., et al. 2025, *ApJ*, 979, 49
- Hayashi, K. 2005, *ApJS*, 161, 480
- Hayashi, K., Abbett, W. P., Cheung, M. C. M., & Fisher, G. H. 2021, *ApJS*, 254, 1
- Hoeksema, J. T., Abbett, W. P., Bercik, D. J., et al. 2020, *ApJS*, 250, 28
- Hollweg, J. V. 1978, *Rev. Geophys.*, 16, 689
- Howard, R. A., Moses, J. D., Vourlidas, A., et al. 2008, *Space Sci. Rev.*, 136, 67
- Jarolim, R., Veronig, A. M., Purkhart, S., Zhang, P., & Rempel, M. 2024, *ApJL*, 976, L12
- Jeong, H.-J., Moon, Y.-J., Park, E., & Lee, H. 2020, *ApJL*, 903, L25
- Jeong, H.-J., Moon, Y.-J., Park, E., Lee, H., & Baek, J.-H. 2022, *The Astrophysical Journal Supplement Series*, 262, 50
- Jiang, C. & Zhang, L. 2025, *Solar Physics*, 300
- Jiang, C. W., Feng, X. S., Bian, X. K., et al. 2023
- Jin, M., Manchester, W. B., van der Holst, B., et al. 2017, *ApJ*, 834, 173
- Kimpe, D., Lani, A., Quintino, T., Poedts, S., & Vandewalle, S. 2005, in *Proc. 12th European Parallel Virtual Machine and Message Passing Interface Conference*, ed. D. K. B. Di Martino & J. J. Dongarra (Sorrento: Springer), 520–527
- Koskinen, H. E. J., Baker, D. N., Balogh, A., et al. 2017, *Space Sci. Rev.*, 212, 1137
- Kuźma, B., Brchnelova, M., Perri, B., et al. 2023, *ApJ*, 942, 31
- Kwak, Y.-S., Kim, J., Kim, S., et al. 2024, *J. Astron. Space Sci.*, 41, 171
- Lani, A., Quintino, T., Kimpe, D., et al. 2005, in *LNCS 3514, Vol. 1, Computational Science ICCS 2005*, ed. V. S. Sunderan, G. D. van Albada, P. M. A. Sloot, & J. J. Dongarra, Emory University (Atlanta, GA, USA: Springer), 281–286
- Lani, A., Villedieu, N., Bensassi, K., et al. 2013, in *AIAA 2013-2589, 21th AIAA CFD Conference*, San Diego (CA)
- Li, C. X., Feng, X. S., Xiang, C. Q., et al. 2018, *ApJ*, 867, 42
- Li, H. C., Feng, X. S., & Wei, F. S. 2021, *J. Geophys. Res.: Space Phys.*, 126, e2020JA028870
- Linan, L., Regnault, F., Perri, B., et al. 2023, *A & A*, 675, A101
- Linker, J., Downs, C., Caplan, R., et al. 2024, in *EGU General Assembly Conference Abstracts, EGU General Assembly Conference Abstracts*, 4200
- Lionello, R., Downs, C., Mason, E. I., et al. 2023, *ApJ*, 959, 77
- Lionello, R., Linker, J. A., & Mikić, Z. 2008, *ApJ*, 690, 902
- Liu, X. J., Feng, X. S., Zhang, M., & Zhao, J. M. 2023, *ApJS*, 265, 19
- Liu, Y. D., Hu, H. D., Zhao, X. W., Chen, C., & Wang, R. 2024, *ApJL*, 974, L8
- Loeschl, P., Valori, G., Hirzberger, J., et al. 2024, *A & A*, 681, A59
- Mason, E. I., Lionello, R., Downs, C., et al. 2023, *ApJL*, 959, L4
- McClarren, R. G. & Hauck, C. D. 2010, *J. Comput. Phys.*, 229, 5597
- Mikić, Z., Downs, C., Linker, J. A., et al. 2018, *Nature Astronomy*, 2, 913
- Mikić, Z., Linker, J. A., Schnack, D. D., Lionello, R., & Tarditi, A. 1999, *Phys. Plasmas*, 6, 2217
- Mikić, Z., Lionello, R., Mok, Y., Linker, J. A., & Winebarger, A. R. 2013, *ApJ*, 773, 94
- Mok, Y., Mikić, Z., Lionello, R., & Linker, J. A. 2005, *ApJ*, 621, 1098
- Nedal, M., Long, D. M., Cuddy, C., Van Driel-Gesztelyi, L., & Gallagher, P. T. 2025, *A & A*, 695, L24
- Odstrcil, D., Pizzo, V. J., Linker, J. A., et al. 2004, *J. Atmos. Sol.-Terr. Phys.*, 66, 1311, towards an Integrated Model of the Space Weather System
- Owens, M. J., Lockwood, M., & Riley, P. 2017, *Sci Rep*, 7, 41548
- Perri, B., Brun, A. S., Réville, V., & Strugarek, A. 2018, *J. Plasma Phys.*, 84
- Perri, B., Finley, A., Réville, V., et al. 2024, *A & A*, 687, A10
- Perri, B., Kuźma, B., Brchnelova, M., et al. 2023, *ApJ*, 943, 124
- Perri, B., Leitner, P., Brchnelova, M., et al. 2022, *ApJ*, 936, 19
- Petrie, G. J. D., Canou, A., & Amari, T. 2011, *Sol. Phys.*, 274, 163
- Pinto, R. F. & Rouillard, A. P. 2017, *ApJ*, 838, 89
- Poedts, S., Lani, A., Scolini, C., et al. 2020, *J. Space Weather Space Clim.*, 10, 57
- Pomoell, J. & Poedts, S. 2018, *J. Space Weather Space Clim.*, 8, A35
- Powell, K. G., Roe, P. L., Linde, T. J., Gombosi, T. I., & de Zeeuw, D. L. 1999, *J. Comput. Phys.*, 154, 284
- Réville, V., Velli, M., Panasenco, O., et al. 2020, *ApJS*, 246, 24
- Sokolov, I. V., van der Holst, B., Manchester, W. B., et al. 2021, *ApJ*, 908, 172

- Tanaka, T. 1995, *J. Geophys. Res.: Space Phys.*, 100, 12057
- Tóth, G., van der Holst, B., Sokolov, I. V., et al. 2012, *J. Comput. Phys.*, 231, 870
- Upton, L. & Hathaway, D. H. 2014, *Apj*, 780, 5
- Wang, H. P., Guo, J. H., Yang, L. P., et al. 2025a, *A & A*, 10
- Wang, H. P., Poedts, S., Lani, A., et al. 2025b, *A & A*, 694
- Wang, H. P., Xiang, C. Q., Liu, X. J., Lv, J. K., & Shen, F. 2022a, *ApJ*, 935, 46
- Wang, H. P., Yang, L. P., Poedts, S., et al. 2025c, *ApJS*, accepted
- Wang, H. P., Zhao, J. M., Lv, J. K., & Liu, X. J. 2022b, *Chin. J. Geophys.*, 65, 2779
- Wang, Y., Feng, X. S., & Xiang, C. Q. 2019, *Comput. Fluids*, 179, 67
- Xia, C., Teunissen, J., Mellah, I. E., Chané, E., & Keppens, R. 2018, *ApJS*, 234
- Yalim, M. S., Pogorelov, N., & Liu, Y. 2017, *J. Phys.: Conf. Ser.*, 837, 012015
- Yang, L. P., Feng, X. S., Xiang, C. Q., et al. 2012, *J. Geophys. Res.: Space Phys.*, 117
- Yeates, A., Amari, T., Contopoulos, I., et al. 2018, *Space Sci. Rev.*, 214
- Zhao, J., Couvidat, S., Bogart, R. S., et al. 2012, *Sol. Phys.*, 275, 375